

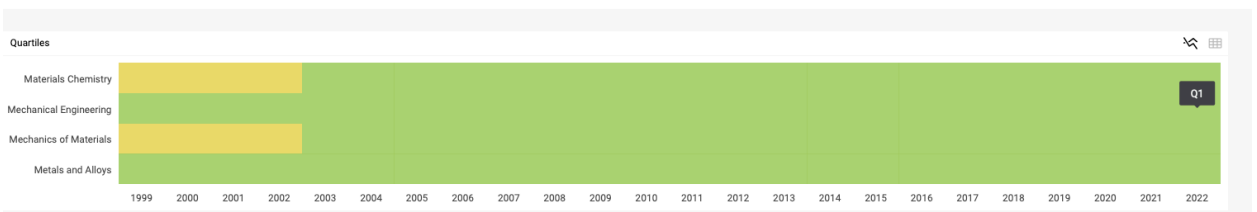
Journal of Alloys and Compounds

COUNTRY	SUBJECT AREA AND CATEGORY	PUBLISHER	H-INDEX
Netherlands Universities and research institutions in Netherlands Media Ranking in Netherlands	Engineering <ul style="list-style-type: none"> Mechanical Engineering Mechanics of Materials Materials Science <ul style="list-style-type: none"> Materials Chemistry Metals and Alloys 	Elsevier BV	200
PUBLICATION TYPE	ISSN	COVERAGE	INFORMATION
Journals	09258388	1991-2023	Homepage How to publish in this journal Contact

SCOPE

- The Journal of Alloys and Compounds is an international peer-reviewed medium for the publication of work on materials comprising compounds as well as alloys. Its great strength lies in the diversity of disciplines which it encompasses, drawing together results from materials science, physical metallurgy, solid-state chemistry and physics. The interdisciplinary nature of the journal is evident in many subject areas. Experimental and theoretical approaches to materials problems require an active interplay between a variety of traditional and novel scientific disciplines. - The journal will not consider topics on liquid alloys, traditional steel, wear, creep, welding and joining, organic materials and polymers, coordination chemistry, ionic liquids, catalysis and biochemistry, it will not consider papers reporting only syntheses without any properties, purely computational papers without sufficient experimental validation, CALPHAD papers without regard to experimental observations. The submission of papers on technology of materials and processing is not encouraged. First principle calculations can only be accepted, if the system has already been proven in experiment or if this is required for a dedicated application. Technical reports will not be accepted. - The work published in the journal should comprise studies on synthesis and structure combined with investigations of chemical and physical properties of alloys and compounds, contributing to the development of areas of current scientific interest. - Papers submitted for publication should contain new experimental or theoretical results and their interpretation. The Journal of Alloys and Compounds provides a unique international forum where materials scientists, chemists and physicists can present their results both to researchers in their own fields and to others active in related areas.

Join the conversation about this journal





Powder plasma arc additive manufacturing of $(\text{AlTi})_{2x}(\text{CoCrNi})_{100-2x}$ medium-entropy alloys: Microstructure evolution and mechanical properties

Jinle Luo^a, Xizhang Chen^{a,*}, Vladislav B. Deev^{b,c,d}, Ming Wen^{d,*}, Yong Shen^e, Sergey Kononov^{a,f}

^a College of Mechanical and Electrical Engineering, Wenzhou University, Wenzhou 325035, China

^b Wenzhou Jinghe Intelligent Manufacturing Science and Technology Company, Wenzhou 325035, China

^c Department of Metal Forming, National University of Science and Technology "MISIS", Moscow 119049, Russian Federation

^d Kunming Institute of Precious Metals, State Key Laboratory of Advanced Technologies for Comprehensive Utilization of Platinum Metals, 650106, China

^e Institute of Metal Research, Chinese Academy of Sciences, 72 Wenhua Road, Shenyang 110016, China

^f Siberian State Industrial University, Novokuznetsk, Kemerovo region—Kuzbas, 654007, Russian Federation

ARTICLE INFO

Keywords:

Additive manufacturing
Directed energy deposition
Medium-entropy alloys
Microstructure
Mechanical properties

ABSTRACT

In this work the effects of Al and Ti element addition on the microstructure and mechanical properties of CoCrNi medium-entropy alloys (MEAs) has been investigated. A novel $(\text{AlTi})_{2x}(\text{CoCrNi})_{100-2x}$ MEAs was fabricated by using powder plasma arc additive manufacturing technique. The influences of Al and Ti elements on the microstructure, mechanical properties and strengthening mechanisms were analyzed by XRD, EBSD and TEM. The $(\text{AlTi})_{2x}(\text{CoCrNi})_{100-2x}$ MEAs exhibited columnar crystal structure, but the average grain size and texture decreased continuously with increasing values of x. Moreover, tensile test results showed that $(\text{CoCrNi})_{90}\text{Al}_5\text{Ti}_5$ alloy possessed strength-ductility balance (yield strength, ultimate tensile strength and elongation to failure of 664 MPa, 897 MPa and 19.3 %, respectively). The analysis on the strengthening mechanism showed that the solid solution strengthening effect was more dominant with increasing of the x in all alloys. $(\text{CoCrNi})_{94}\text{Al}_3\text{Ti}_3$ and $(\text{CoCrNi})_{90}\text{Al}_5\text{Ti}_5$ have similar average grain sizes, wherein the difference in mechanical properties between both the alloys can be mainly attributed to the formation of fine grain sizes. $(\text{CoCrNi})_{90}\text{Al}_5\text{Ti}_5$ has a small amount of dislocations, solid solution strengthening and grain boundary strengthening are the main sources of the excellent properties.

1. Introduction

High entropy alloys (HEAs) and medium entropy alloys (MEAs) comprise of multi-principal elements and have attracted significant attention in recent years [1,2]. Different from traditional alloys, the mixing entropy of HEAs/MEAs is higher, which will prefer to form stable and simple solid solution phases such as face-centered cubic (FCC), body-centered cubic (BCC), and hexagonal close-packed (HCP) [3,4]. In addition, HEAs/MEAs have four major effects, including high entropy of mixing, lattice distortion, sluggish diffusion, and cocktail effects [5,6]. All these characteristics result in outstanding mechanical properties in HEAs/MEAs, such as excellent tensile properties [7,8], superior wear resistance [9,10], corrosion resistance [11,12], and good magnetic

properties [13,14]. Recently, the single-phase FCC CoCrNi MEA with excellent plasticity has attracted extensive research interest [15–17]. However, CoCrNi MEA possesses excessive ductility, but its strength is insufficient for engineering applications. Therefore, an effective method to achieve the balance in strength and ductility is highly needed.

The conventional route such as arc melting, casting and spark plasma sintering are popularly employed to fabricate CoCrNi-based MEA [18–20]. For example, Liu et al. developed a complex structure of CoCrNi-based aggregates with non-recrystallized phase by using cold-rolled and annealing. The aggregates recrystallized in fine grains with precipitated phases and found to possess ultimate tensile strength of 1304 MPa and elongation of 22 % [21]. Meanwhile, Sathiyamoorthi et al. fabricated ultra-fine-grained CoCrNi MEAs by high-pressure

* Corresponding author.

E-mail addresses: chenxizhang@wzu.edu.cn, Kernel.chen@gmail.com (X. Chen).

<https://doi.org/10.1016/j.jalcom.2023.172474>

Received 17 July 2023; Received in revised form 6 October 2023; Accepted 9 October 2023

Available online 10 October 2023

0925-8388/© 2023 Elsevier B.V. All rights reserved.

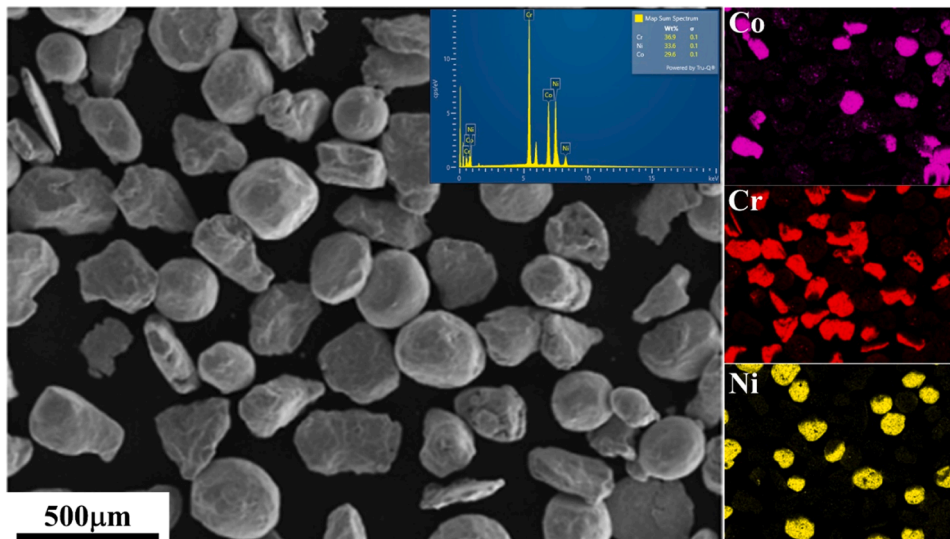


Fig. 1. SEM micrographs of CoCrNi powder and element mapping.

torsion and annealing with yield strength of approximately 1.4 GPa and uniform elongation of 24 % [22]. Literature reveals that suitable post fabrication treatment can improve strength and plasticity, but the fabrication route for these alloys remain complex and hinder their commercial viability. The rapid development of additive manufacturing (AM) provides a new way to prepare HEA/MEAs [23–26]. The AM generates work paths directly from the CAD models and builds the components by layer-by-layer deposition [27,28]. Among a large of AM technologies, selective laser melting (SLM) [29–31], laser-direct energy deposition (L-DED) [25,32,33], selective electron beam melting (SEBM) [34], wire arc additive manufacturing (WAAM) [35] and powder plasma arc additive manufacturing (PPA-AM) are found to be successful and popular [36]. Currently, many researchers have begun to investigate CoCrNi using AM technologies. Such as, Niu et al. prepared CoCrNi MEA by using SLM, and the results showed that the increase of volumetric energy density will lead to the increase of the average grain size and

residual stress of the alloys [37]. Han et al. produced CoCrNi via AM with excellent mechanical properties at cryogenic temperatures (ultimate tensile strength of 1340 MPa), and the high strength originated from the cellular structures and the complex heterogeneous columnar grains [38]. Meanwhile, Xue et al. fabricated CoCrNi-based MEAs by using L-DED, and the results showed that the addition of Mo and WC would effectively promote the grain refinement and solid solution strengthening [39]. Compared with other AM methods, PPA-AM is a novel DED technology with low price and high molding efficiency, which uses ultra-high energy density plasma arc as the heat source and alloy powder as the raw material. The rapid solidification and cyclic annealing during PPA-AM process endows the alloys with unique microstructure and special properties. For example, Zhang et al. studied the effect of equal atomic radius elements (Al, Nb, Ta) on the microstructure of CoCrFeNi. It was found that the addition of high melting point elements had a significant effect on the formation of the solid

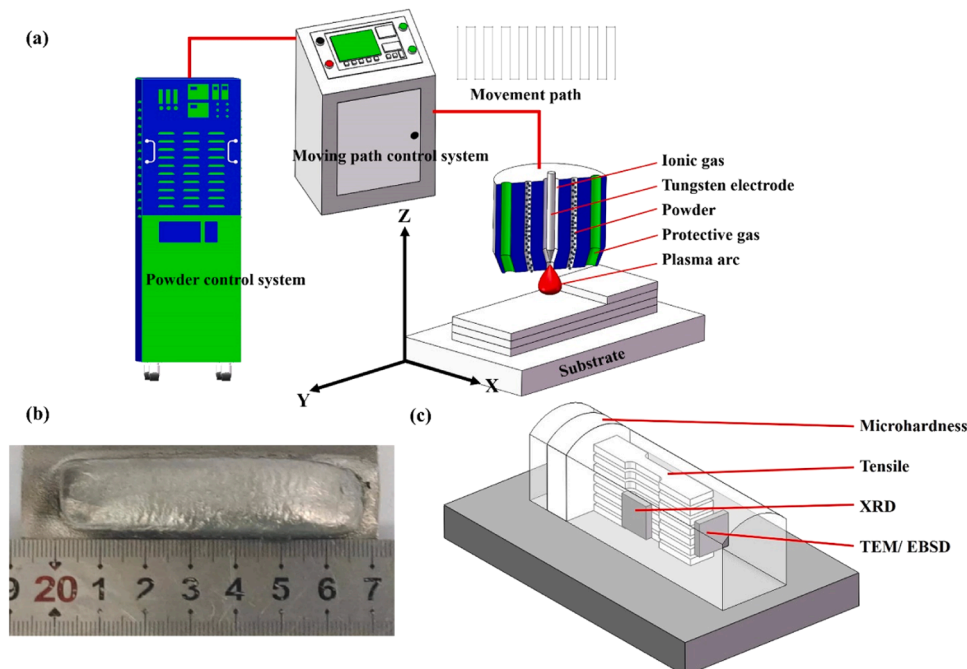


Fig. 2. (a) Schematic diagrams showing the PPA-AM system, (b) Diagram of the sample locations tested, (c) Representative samples via PPA-AM deposition.

Table 1
Key preparation parameters of the $(\text{AlTi})_{2x}(\text{CoCrNi})_{100-2x}$ MEAs.

Parameter	Value
Substrate thickness	10 mm
Torch to substrate distance	10–12 mm
Ionic gas	2.5–3.0 L/min
Powder feeding gas	2.0–2.5 L/min
Protective gas	10–15 L/min
Preheating current	60 A
Deposition current	110 A
Powder feeding rotor speed	20 r/min
Dwell time between layer	3–4 min
Scanning speed	25 mm/min

solution phase of topologically closed packed (TCP) [40]. Shen et al. fabricated $\text{Al}_{1.2}\text{CoCrFe}_{2.1}$ dual-phase HEA by using PPA-AM. The authors applied heat treatment assisted precipitation characteristics of FCC and B2 phases and investigated their effect on mechanical properties [41]. Although numerous studies have been reported on the microstructural evolution of AM HEAs/MEAs [31,39,42–45], studies on the PPA-AM CoCrNi-based MEAs conditions are scarce, restricting their practical engineering applications.

In this paper, the bulk $(\text{AlTi})_{2x}(\text{CoCrNi})_{100-2x}$ MEAs with high-purity mixed powder of five elements were successfully manufactured by PPA-AM. Among the five elements in the Co–Cr–Ni–Al–Ti system, Al and Ti were the largest atomic radius elements. The addition of Al and Ti in the CoCrNi matrix was done to promote the solid solution strengthening of the alloys. The microstructural and mechanical property characterization of the as-built MEAs was investigated intensively. A superior combination of strength and ductility was obtained without any post treatment.

2. Material and methods

2.1. Materials preparation

In this study, gas atomized high-purity (>99.5 % purity) Co, Cr, Ni, Al, and Ti elemental powders were used with particle sizes ranging from 53 to 150 μm . To improve homogeneity of blend, all metal powders were initially mixed in a high-energy ball mill (YXQM12L, MITR Ltd, Hunan, China) for 8 h, subsequently vacuum dried in an oven for 100 min. The weight ratio of Al_2O_3 ceramic balls (10 mm diameter) to powder was 2:1, with a grinding speed of 100 r/min. When the powders were blended, enough argon gas should be filled in the tank as the protective gas to avoid oxidization of the metal powders. Fig. 1 shows the SEM micrographs of CoCrNi powders after ball milling. The mixed powders are nearly spherical or spherical with particle sizes of about 50–120 μm . The inserted EDS X-ray specimens in Fig. 1 indicate that the mixed powders are composed of three high-purity Co, Cr and Ni elemental

powders. In addition, the elemental mapping showed the relatively uniform distribution of the three elements in the blended powders.

As shown in Fig. 2(a), the PPA-AM equipment (DML-VO3AD, Duomu Company, Shanghai, China) was composed of a powder control system and a moving path control system. The PPA-AM process was performed under the reciprocating oscillating scanning path. The deposition current was 110 A, the scanning speed was 25 mm/min, and the flow rate of powder feeding gas (high purity argon) was 2.0 L/min. The specific processing parameters were presented in Table 1. Before the deposition experiments, the substrate surface was cleaned by ethanol to remove surface contaminants, and then polished with a grinding wheel. Meanwhile, the substrate was preheated for 4–6 min to ensure the MEA was tightly bonded on the substrate. During the AM process, each layer was sanded by grinding wheel after the deposition to ensure the good bonding between the layers. Finally, eight-layer thick walls were deposited to the approximate sizes of 60 mm \times 18 mm \times 20 mm (length \times width \times height) on the SUS304 stainless steel substrate (as shown in Fig. 2(b)). The $(\text{AlTi})_{2x}(\text{CoCrNi})_{100-2x}$ MEAs ($x = 0, 3, 5, 7$) samples were denoted as CoCrNi, Al_3Ti_3 , Al_5Ti_5 and Al_7Ti_7 , respectively.

2.2. Microstructural characterization

Fig. 2(c) shows the schematic of sampling for testing of mechanical properties and microstructure. Before the tests, the specimens were polished with 320#, 600#, 800#, 1000#, 1200#, 1500#, 2000# SiC sandpapers followed by polishing with W0.25 diamond spray. Phase characterizations were performed by using XRD analysis in a Rotating Anode X-ray Powder Diffractometer (XRD: BRUKER D8 Advance), which emitted the Cu $K\alpha$ radiation and operated at 40 kV with 150 mA. An increment of 0.01° and the scan rate of $5^\circ/\text{min}$ over the 2θ range of $20\text{--}100^\circ$ were used for XRD analysis. The microstructure was investigated by using electron back scatter diffraction (EBSD, Oxford Nordly Max3, Oxford Instrument Technology Co, Ltd.). Transmission Electron Microscopy (TEM) analyses were carried out using a JEM F200 TEM device operating at 200 kV.

2.3. Mechanical testing

The Vickers hardness of the polished samples was measured using HVS-1000A hardness tester at a load of 9.8 N for 15 s. The tests were carried out at intervals of 1 mm along the build direction, and the average value of three measurements was used. Prior to the tensile test, the alloy samples were ground to remove the surface oxide layers by using SiC sandpapers. The dog-bone shaped tensile test specimens were tested at room temperature (RT) by using the universal testing machine (instron 5900) at a strain rate of 10^{-3} s^{-1} . Tensile tests were tested three times to ensure the accuracy of the experiment.

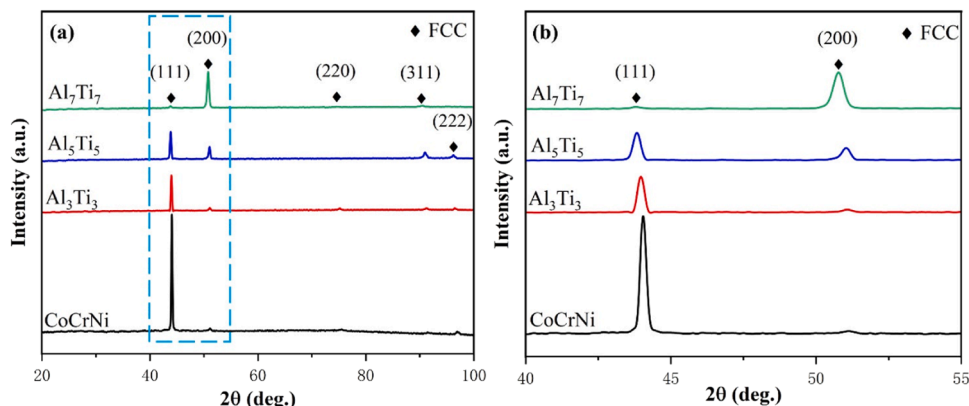


Fig. 3. (a) XRD pattern of $(\text{AlTi})_{2x}(\text{CoCrNi})_{100-2x}$ MEAs, (b) enlarged view of FCC₍₁₁₁₎ and FCC₍₂₀₀₎ peaks.

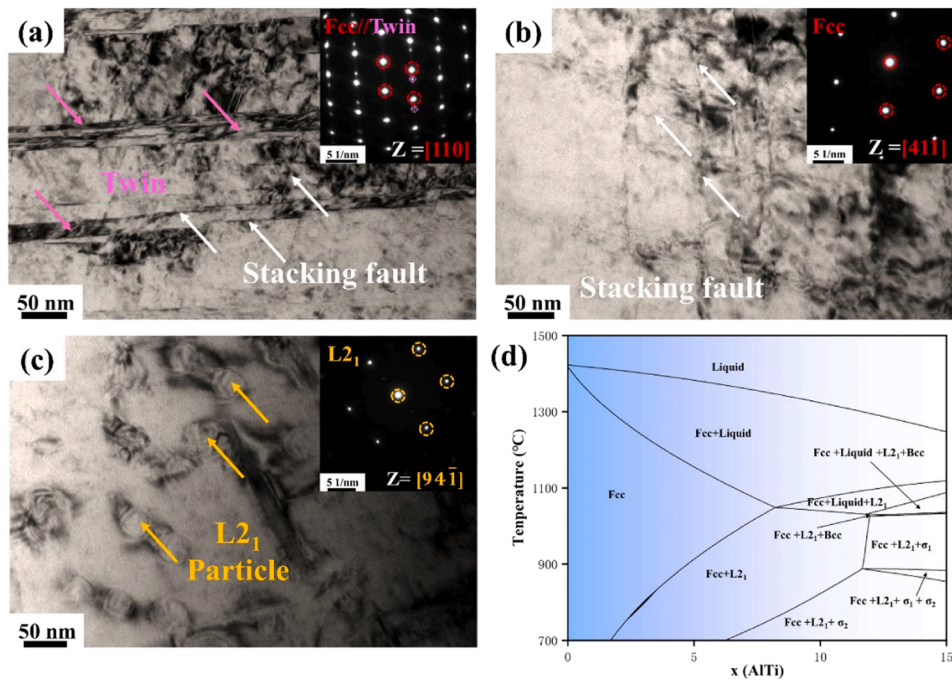


Fig. 4. TEM images of the MEAs with the corresponding SAEDs: (a) Al_3Ti_3 ; (b) Al_5Ti_5 ; (c) Al_7Ti_7 . (d) Phase diagram of $(\text{AlTi})_x(\text{CoCrNi})_{100-x}$ MEAs.

3. Results and discussion

3.1. Microstructures

Fig. 3(a) shows the XRD patterns of the $(\text{AlTi})_{2x}(\text{CoCrNi})_{100-2x}$ MEAs. It is evident that all the samples exhibit typical single phase FCC structure and no diffraction peaks of the second phase are obvious. In addition, the diffraction peak intensity of $\text{FCC}_{(111)}$ and $\text{FCC}_{(200)}$ show different results with the increase of Al and Ti contents. The diffraction peak intensities of $\text{FCC}_{(111)}$ gradually decreases, while that of $\text{FCC}_{(200)}$ gradually increases. The local magnification pattern of the diffraction peaks of $\text{FCC}_{(111)}$ and $\text{FCC}_{(200)}$ is shown in Fig. 3(b). Obviously, the diffraction peaks of $\text{FCC}_{(111)}$ and $\text{FCC}_{(200)}$ shifted gradually towards the lower 2θ angle as x increased. In addition, we also noticed that the XRD diffraction peaks of MEAs broadened with the increase of Al and Ti contents. Through Scherrer equation, it can be judged that the addition of Al and Ti will promote the decrease of grain size. The lattice constants for CoCrNi , Al_3Ti_3 , Al_5Ti_5 and Al_7Ti_7 were calculated by Jade 6 software and were found to be 3.5643 Å, 3.5741 Å, 3.5836 Å and 3.5958 Å, respectively. Those trends can be attributed to the larger atomic radii of Al and Ti (Co (0.1251 nm), Cr (0.1246 nm), Ni (0.1246 nm), Al (0.1432 nm), Ti (0.1462 nm)). These are dissolved in the CoCrNi matrix as solutes, leading to lattice distortion and increase in lattice constants of the alloys [18,46]. Increase in the Al and Ti atoms that occupy lattice positions, results in the increase in lattice distortion energy and resistance to dislocation movement, which results in the enhancement of strength and hardness of the MEAs.

To further analyze the microstructures of MEAs, TEM characterization was done as shown in Fig. 4. The bright-field (BF) TEM (Fig. 4(a)) images of the Al_3Ti_3 MEA and the corresponding selected area electron diffraction (SAED) show that the alloy consists of single FCC phase. In addition, a large number of twins and stacking fault were observed in Al_3Ti_3 . It might stem from the CoCrNi matrix having extremely low stack fault energy, and local heating and rapid cooling during the AM process [15,22,47,48]. As can be seen in Fig. 4(b), with the increase of Al and Ti content, Al_5Ti_5 still has single FCC structure, while the twins disappear and stacking faults decrease. Further in the Al_7Ti_7 alloy, the presence of second phase particles is observed in Fig. 4(c), which is derived from the

SAED as L_{21} ($\text{Ni}_2(\text{AlTi})$). The generation of phase significantly enhances the strength of the alloy but also leads to decrease in plasticity [8,18,20]. In order to reveal the effects of Al and Ti on microstructure evolution, an equilibrium phase diagram of CoCrNi with varying (AlTi) content was calculated using pandat software, and the result is shown in Fig. 4(d). The equilibrium phase diagram indicates that all MEAs would generate brittle L_{21} metallic phases at 900 °C, while Al_3Ti_3 and Al_5Ti_5 were not formed in the present experiments. This difference is mainly attributed to the following two points: the rapidly cooling of AM and the sluggish diffusion effect of HEAs/MEAs will effectively inhibit the generation of second phases, such as L_{12} phase, sigma phase [49,50]. Besides, the process of additive manufacturing causes the loss of Al elements, which leads to a leftward shift of the actual composition.

Fig. 5 shows the EBSD data for $(\text{AlTi})_{2x}(\text{CoCrNi})_{100-2x}$ MEAs cross section taken in the building direction. IPFs and average grain size maps are shown in Fig. 5(a–f). The IPFs show that MEAs have columnar FCC crystals along $\langle 001 \rangle$, which is due to the preferred growth direction of FCC crystals being $\langle 001 \rangle$. AM has a layer-by-layer stacking characteristic, which has the largest temperature gradient in the building direction. The FCC grains grow continuously along the heat transfer gradient direction, leading to formation of columnar crystals of MEAs along the build direction [24,32]. In addition, the polar figures (PFs) in Fig. 6 also show that all MEAs have the typical features of $\{100\}$ fiber textures. This result matches well with the evolution of the XRD characteristic peaks in Fig. 3, which indicates that the main diffraction peak (111) in the MEAs, gradually decreases with the increase of the (200) diffraction peak. According to the statistical results based on EBSD data, the grain size of the PPA-AM fabricated MEAs samples exhibited some heterogeneity in the range of 30–730 μm . Such a grain morphology may be attributed to the build direction with inhomogeneous temperature distribution and variations in the existing temperature gradients [51]. In the building direction, the scan paths of two adjacent layers of the sample were repeatedly heated and remelted, and the distance of the plasma heat source from the sample caused different cooling rates [27,40]. With the increase of Al and Ti contents, the grain size of FCC decreases significantly. The average grain sizes of Al_3Ti_3 , Al_5Ti_5 and Al_7Ti_7 were 115.70 μm , 114.25 μm , and 63.88 μm , respectively. In addition, the proportion of fine grain size (less than 50 μm) in the alloy increases

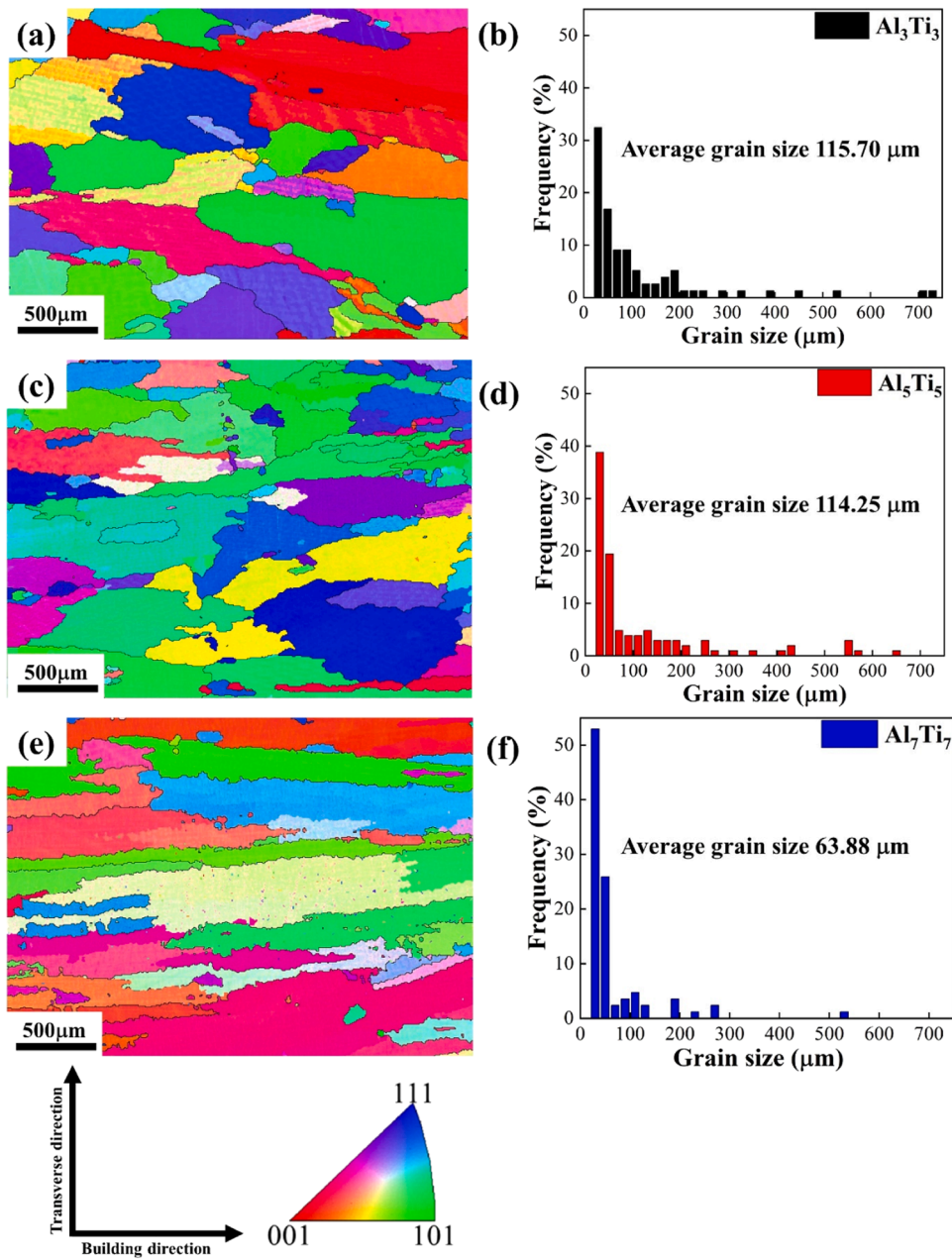


Fig. 5. EBSD data of $(AlTi)_{2x}(CoCrNi)_{100-2x}$ MEAs with different Al and Ti addition: IPFs map and grain size distribution (a, b) Al_3Ti_3 ; (c, d) Al_5Ti_5 ; (e, f) Al_7Ti_7 .

significantly with the increase of Al and Ti content in this system, which are 49.35 %, 58.25 % and 78.83 %, respectively. Al and Ti elements are forced out of the solid-liquid interface during solidification and produce greater constitutive subcooling [52,53]. The accumulation of elements in front of the solid-liquid interface may reduce the grain growth rate and lead to the formation of finer grains.

To further investigate the differences in the AM-prepared MEAs, the kernel average misorientation (KAM) maps and the corresponding local misorientation distribution maps obtained from EBSD are shown in Fig. 7. As known, the KAM is widely used to show the local deformation or dislocation density of alloy materials [54,55]. An analysis of the KAM maps, as shown in Fig. 7(a), (c) and (d), reveals a relatively high KAM values distribution in the grains of Al_3Ti_3 , while the KAM values of Al_7Ti_7 are lower. This reveals that the stress in region Al_3Ti_3 is higher than the one in region Al_7Ti_7 . In this study, we used the KAM method to determine the local orientation difference from the EBSD orientation data. Any calculated local misorientation angle greater than 2° was

excluded. The local misorientation of a point ($100\text{ nm} \times 100\text{ nm}$) was determined based on its surrounding 24 points as follows [54]:

$$\Delta\theta_i = \frac{1}{n} \sum_{j=1}^n |\theta_j^{sur} - \theta_i|$$

where θ_i represents the local misorientation at the point 'i' and θ_j^{sur} is the misorientation at its neighboring point 'j'. From the obtained values of the local misorientation at a different point, the density of geometrically necessary dislocation (GND) can be derived using the following [54]:

$$\rho_{GND} = \frac{2\Delta\theta_i}{\mu b}$$

where ρ_{GND} is the GNDs density, $\mu = 6.0\ \mu\text{m}$ is the unit length, and the Burgers vector b is derived from XRD measured lattice constants. Thus, the GND densities can be calculated to be approximately $8.15 \times 10^{12}\ \text{m}^{-2}$, $6.91 \times 10^{12}\ \text{m}^{-2}$, $6.02 \times 10^{12}\ \text{m}^{-2}$. It shows that the Al_3Ti_3 region

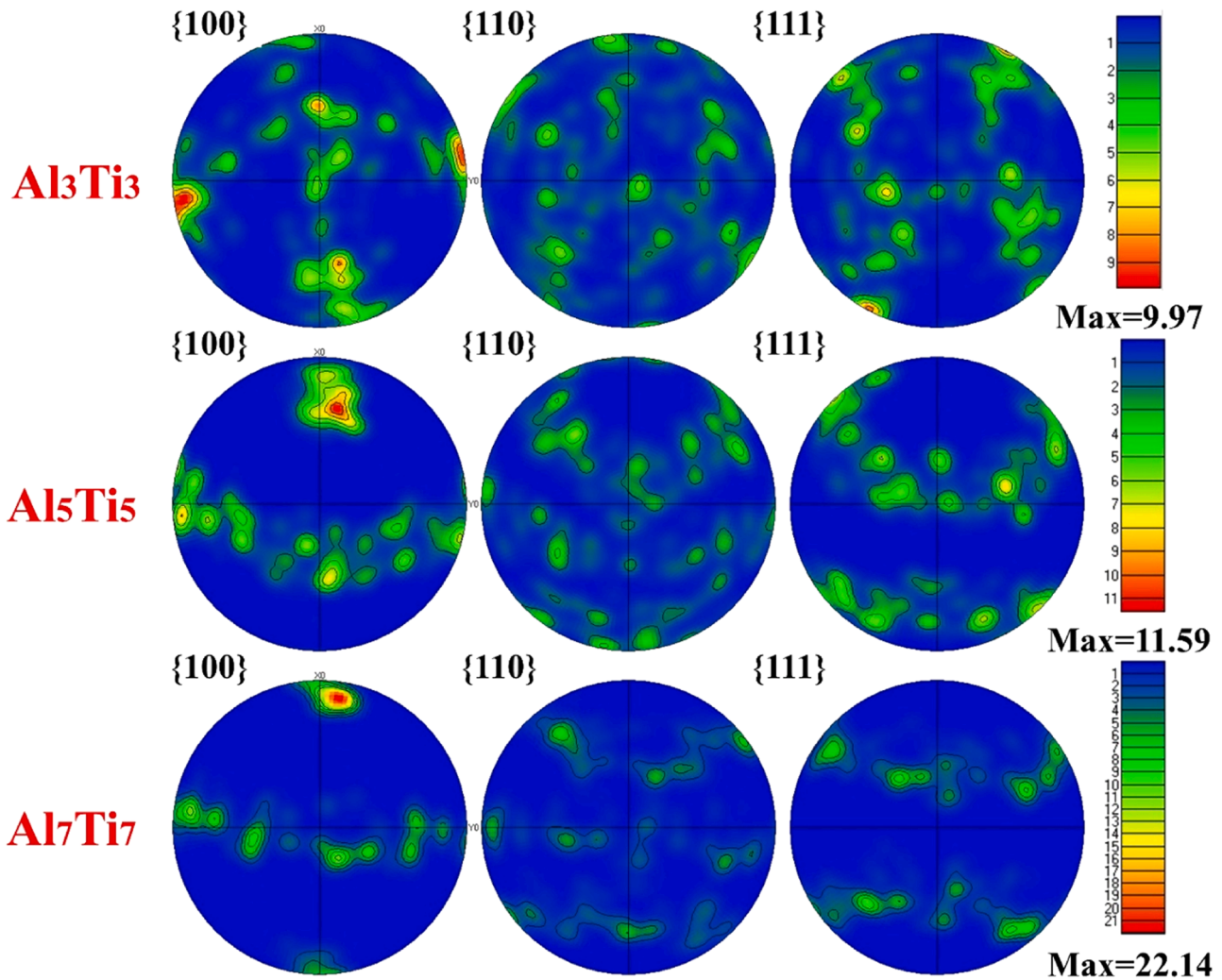


Fig. 6. Pole Figures of the $(\text{AlTi})_{2x}(\text{CoCrNi})_{100-2x}$ MEAs.

has a higher ρ_{GND} than the others. This means that large local misorientation generates high density of GNDs. The mobility of dislocations is reduced by the increase of Al and Ti content.

3.2. Mechanical properties

The microhardness plots of the PPA-AM $(\text{AlTi})_{2x}(\text{CoCrNi})_{100-2x}$ MEAs are shown in Fig. 8(a) and the plots of average microhardness values are plotted in Fig. 8(b). Obviously, the Al and Ti content has a significant influence on the microhardness of the MEAs. It is evident that an increase of the x value increases the average microhardness value from 180 HV ($x = 0$), 264 HV ($x = 3$) to 350 HV ($x = 5$) and eventually to 440 HV ($x = 7$). In addition, it can also be seen from Fig. 8(a) that the microhardness of the MEA specimens made by PPA-AM is stable and relatively uniform.

Fig. 8(c) shows the uniaxial tensile engineering stress-strain curves of the MEAs. The yield strength (YS), ultimate tensile strength (UTS) and elongation to failure (EF) are summarized in Table 2. According to these data, it can be shown that the MEAs prepared in this experiment have stable tensile properties. Moreover, it can be observed that the addition of Al and Ti promotes the increase of MEA strength, but the plasticity is reduced. Among them, CoCrNi MEA exhibited low strength (206 MPa for YS and 541 MPa for UTS) and excellent plasticity (51.4 % for EF). when $x = 3$, the Al_3Ti_3 alloy exhibited relatively excellent EF of 41.2 % with relatively values of lower YS (412 MPa) and UTS (752 MPa). It can be observed further that when $x = 5$, the YS of MEA increased

significantly to 665 MPa while the UTS increased to 898 MPa, but the EF reduced drastically (19.3 %). As the value of x increased to 7, the alloy becomes brittle. The YS and UTS of the Al_7Ti_7 alloy are 808 MPa and 1004 MPa, respectively, but the EF was only 6.2 %. The tensile properties of the present MEAs and other reported HEAs/MEAs materials are summarized in the Ashby map in Fig. 8(d). The results clearly indicate that the present MEAs show an outstanding strength-ductility combination, which is better than most other metallic materials.

Fig. 8(e) and (f) show the true stress-strain curves and the corresponding strain hardening rate curves of the MEAs. The strain hardening rate of the MEAs can be roughly divided into three stages: Stage I, elastic-plastic transition stage; Stage II, hardening stage; and Stage III, failure stage. In Stage I, the strain hardening rates of all samples dropped dramatically owing to the transition from the elastic stage to the plastic stage. During Stage II, the strain hardening rate curves displayed a significant transient nature. Secondary strain hardening makes the alloys have a high level of hardening ability. As shown in Fig. 4, all the MEAs have a heterogeneous structure with different grain sizes, which are remarkable with the increase of Al and Ti contents. The heterogeneous structure promotes heterogeneous deformation-induced (HDI) hardening, causing transient hardening behavior [56,57]. In Stage III as the value of true stress crosses UTS, the strain hardening rate decreases again and Al_7Ti_7 fractures quickly without undergoing significant necking compared with specimen Al_3Ti_3 . The mechanical properties and work-hardening ability are attributable to the interaction of dislocations and twins in the alloys. The twins provide barriers to dislocation

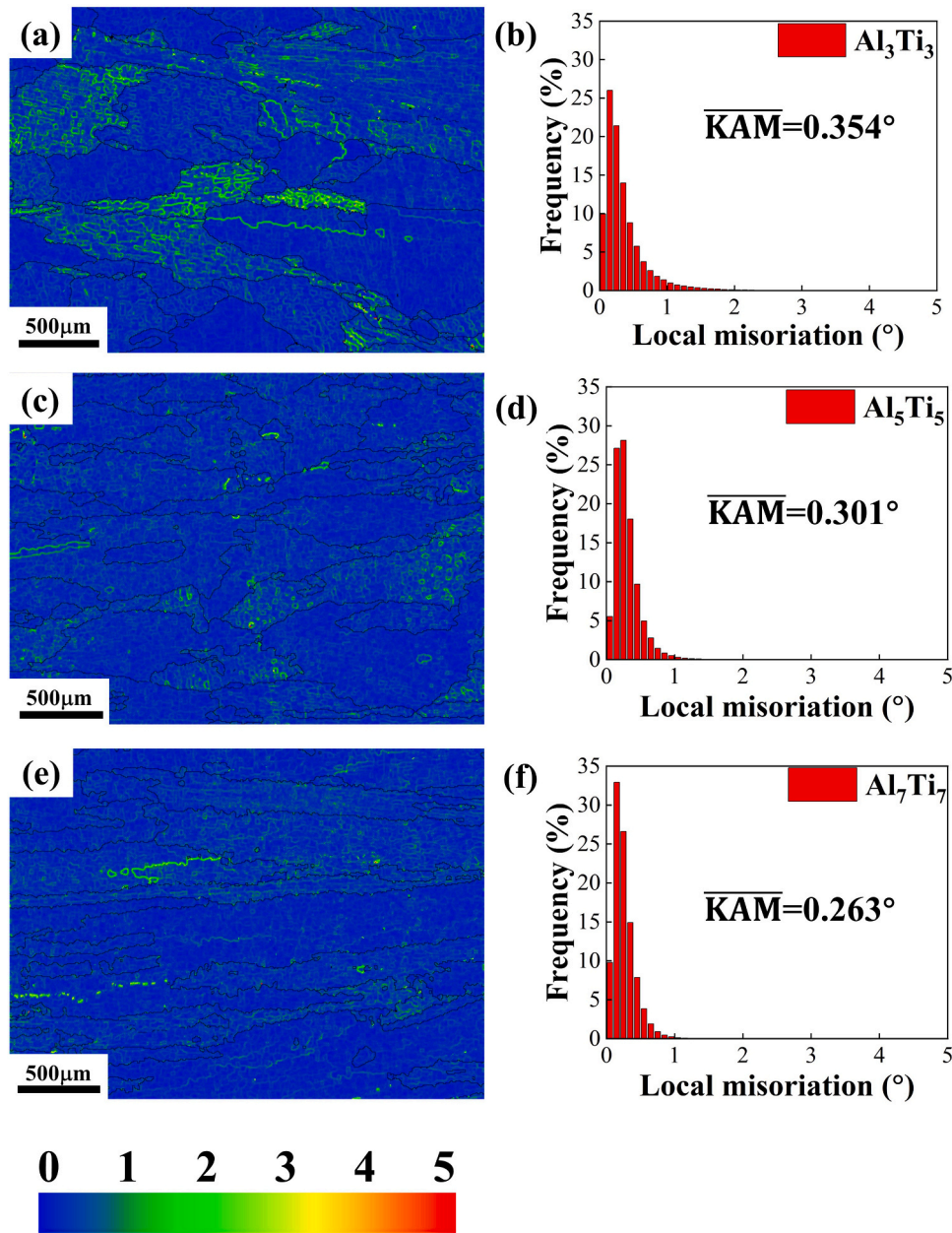


Fig. 7. KAM maps and the corresponding local misorientation distribution maps of the MEAs: (a, b) Al_3Ti_3 ; (c, d) Al_5Ti_5 ; (e, f) Al_7Ti_7 .

movement and promote the build-up of dislocations within the twins during the tensile processes [58,59].

3.3. Strengthening mechanisms

The strengthening mechanisms of HEAs/MEAs can be classified into four types: solid solution strengthening, grain boundary strengthening, dislocation strengthening and precipitation strengthening [6,57]. Solid solution strengthening caused by lattice distortion was considered to be the dominant mechanism when elements with large atomic radii were added to the CoCrNi-matrix [19,21,46]. Precipitation strengthening is due to the restriction in dislocation offered by the second phase particles [20,40,52]. The strengthening contribution from the grain boundaries can be deduced from the classic Hall–Petch relationship in which the grain boundary impedes the dislocation. Small grain size has larger grain boundary area thereby contributing to higher strength. The dislocation strengthening has an inseparable relationship with grain size or inter-phase boundaries [20,22].

In the present study, large-size atoms dissolved in the CoCrNi matrix resulted in solid solution strengthening due to lattice distortion. According to the XRD and TEM results, it was found that no precipitation phase was generated in Al_3Ti_3 and Al_5Ti_5 alloys, and L_{21} precipitation phase was generated in Al_7Ti_7 , indicating that Al and Ti have been dissolved in the FCC matrix. The relative degree of lattice distortion incurred in the alloys can be calculated by δ , which is used to describe the atomic size mismatch. Considering that the FCC is the single phase present in the MEA, the atomic size mismatch of the FCC phase in MEAs can be calculated according to the following equation [60]:

$$\delta = \sqrt{\sum_{i=1}^n c_i \left(1 - \frac{r_i}{\bar{r}}\right)^2}$$

Here, c_i is atomic percentage of the i -th element in FCC phase, r_i is the atomic radii of i -th element and $\bar{r} = \sum_{i=1}^n c_i r_i$ is the average atomic radius. The atomic size mismatch of the FCC phase in $(\text{AlTi})_{2x}(\text{CoCrNi})_{100-2x}$ ($x = 0, 3, 5, 7$) are 0.16 %, 3.75 %, 4.71 % and

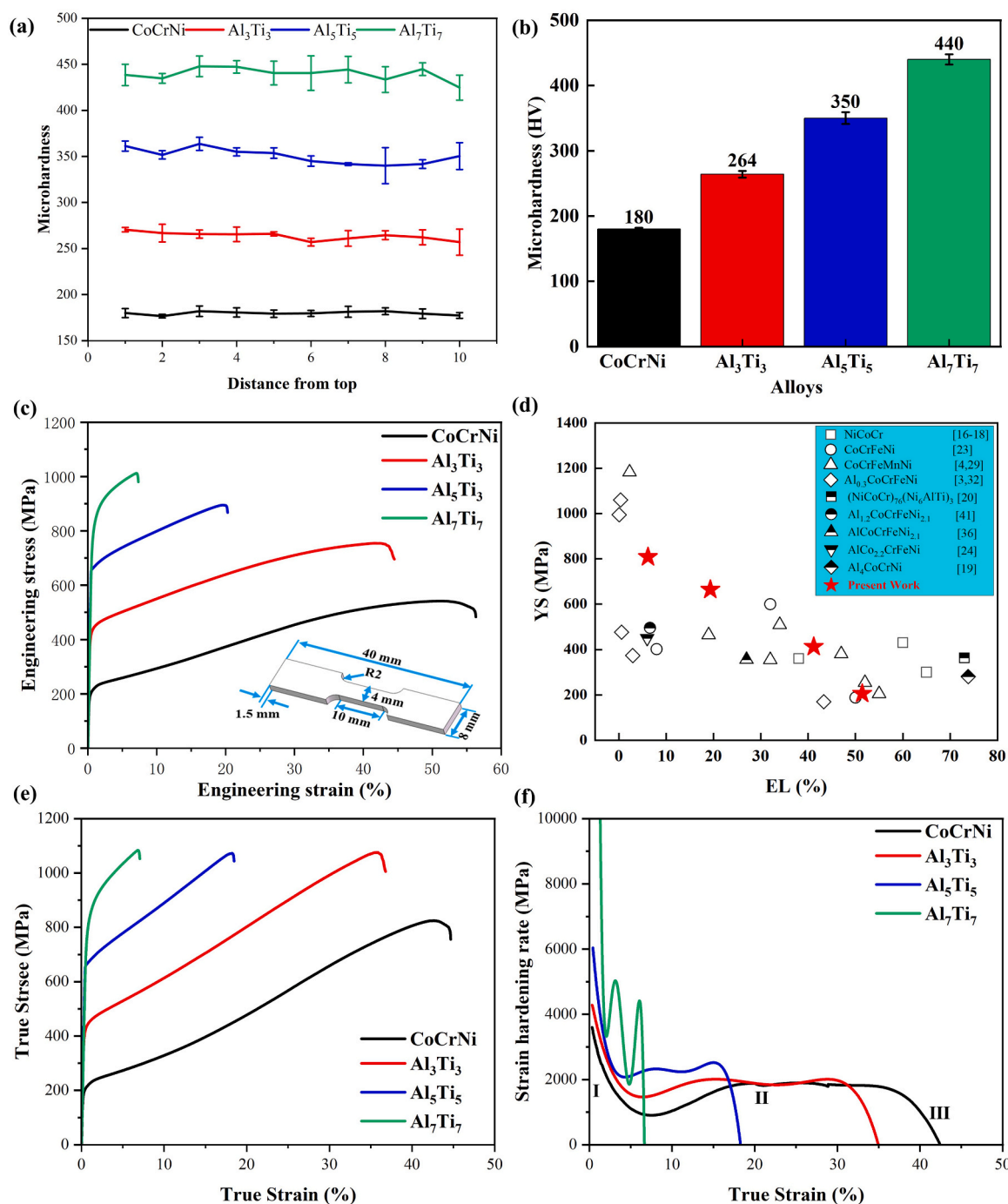


Fig. 8. Mechanical properties of (AlTi)_{2x}(CoCrNi)_{100-2x} MEAs prepared by PPA-AM: (a) microhardness of different x content; (b) The average microhardness of each MEAs; (c) engineering stress-strain curves; (d) yield strength-elongation Ashby plots of the reported HEAs/MEAs at RT [3,4,16–20,23,24,29,32,36,41]; (e) true stress-strain curves; (f) strain hardening rate curves.

Table 2
Mechanical properties of the PPA-AM deposited (AlTi)_{2x}(CoCrNi)_{100-2x} MEAs.

Alloys	YS (MPa)	UTS (MPa)	EF (%)
CoCrNi	206 ± 8	541 ± 1	51.4 ± 0.5
Al ₃ Ti ₃	412 ± 4	752 ± 5	41.2 ± 0.7
Al ₅ Ti ₅	665 ± 8	898 ± 4	19.3 ± 0.4
Al ₇ Ti ₇	808 ± 31	1004 ± 9	6.2 ± 1.2

5.41 %, respectively. It is apparent that the large solute atoms of Al and Ti in the FCC phase causes greater atomic size mismatches. Precipitation strengthening refers to the strengthening of the alloy by second phase particles. The L₂₁ precipitated phase was significantly observed in Al₇Ti₇ (Fig. 4(c)). According to the reported literature as well, the L₂₁ precipitated phase can effectively impede dislocation slip during stretching, which can improve the strength of the alloy [50,57]. As can be seen in Table 2, minor amounts of Al and Ti dissolved in MEA significantly enhance the YS and UTS of the alloys ((CoCrNi) to (CoCrNi)₉₀Al₅Ti₅), but excessive amounts produce brittle L₂₁, which has a very limited enhancement in strength. In addition, Fig. 8(b) shows that

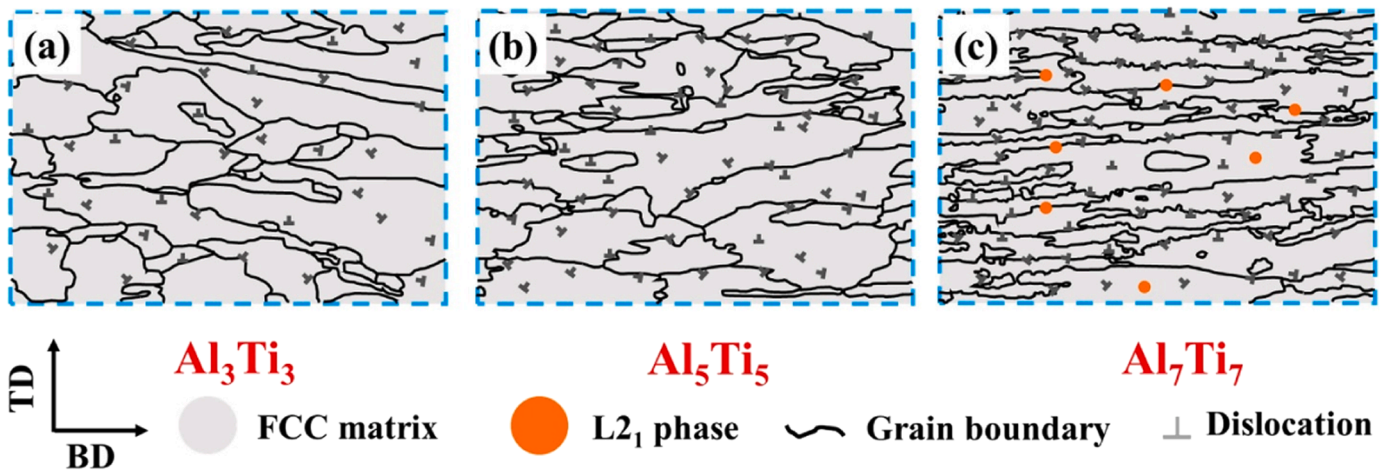


Fig. 9. Schematic diagram of microstructure evolution in Co-Cr-Ni-Al-Ti MEAs with different Al and Ti elemental content: (a) Al_3Ti_3 ; (b) Al_5Ti_5 ; (c) Al_7Ti_7 .

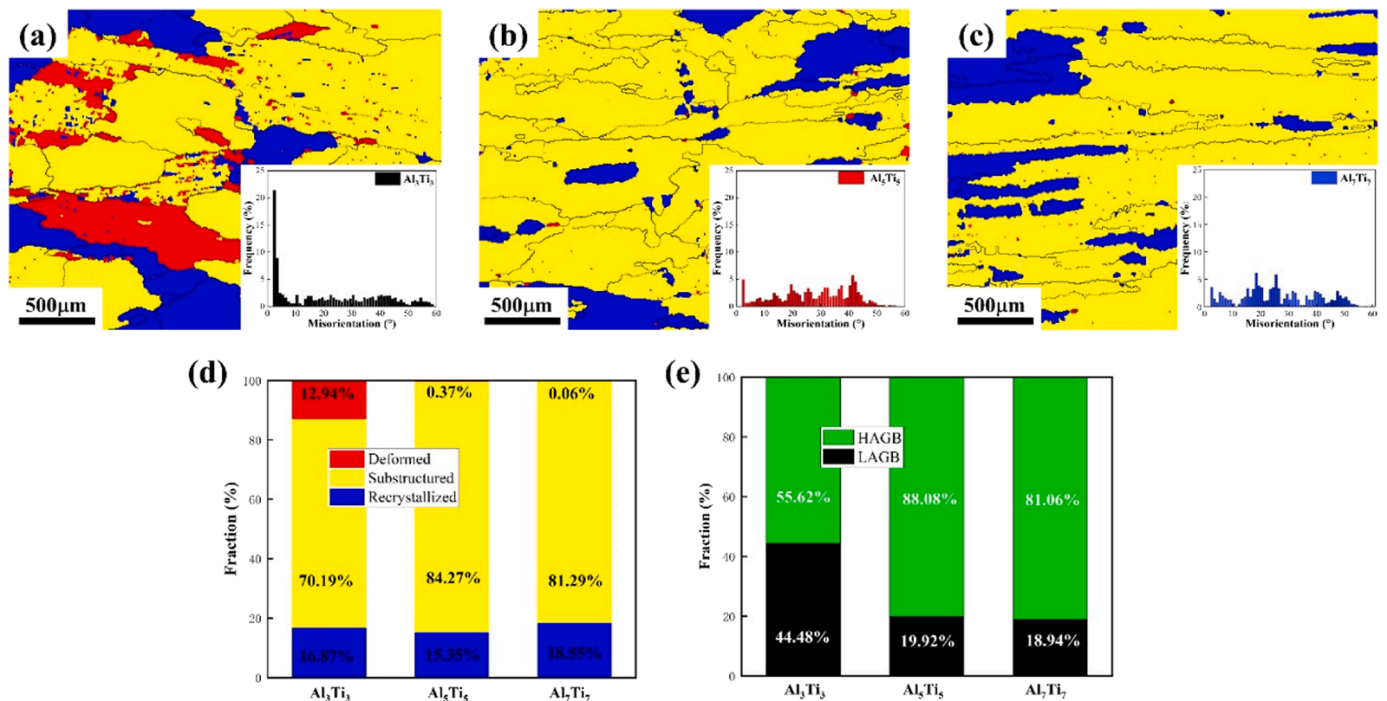


Fig. 10. IAMA map and misorientation angle distribution of $(\text{AlTi})_{2x}(\text{CoCrNi})_{100-2x}$ ($x = 3, 5, 7$) MEAs: (a) Al_3Ti_3 , (b) Al_5Ti_5 , (c) Al_7Ti_7 , (d) volume fraction of the deformed, substructured, and recrystallized structures (e) volume fraction of HAGB and LAGB.

the microhardness of the alloy increases significantly with the strength of the alloy. It is interesting to note that the microhardness varies linearly with an interval of 45 HV for every unit increase in the value of x over a certain range. These results indicate that solid solution strengthening has a significant effect on MEAs.

As can be seen from XRD, Fig. 5 and Fig. 9, the grain size of the alloy changes significantly, indicating the necessity of discussing the effect of grain boundary strengthening on MEAs. Grain boundary strengthening, is often used in conventional processes to enhance the mechanical properties of materials by cold work. In grain boundary engineering, the effect of grain boundary strengthening on mechanical properties can be determined qualitatively in terms of the volume fraction of orientation angle distribution [61]. The misorientations of the grain boundaries higher than 15° are defined as high-angle grain boundaries (HAGBs) and those $<15^\circ$ are called as low-angle grain boundaries (LAGBs) [62]. Combined details of XRD, Fig. 5, Fig. 9 and Fig. 10(e), it can infer that in

comparison to CoCrNi and Al_3Ti_3 MEA, the Al_5Ti_5 and Al_7Ti_7 have finer grains and with larger percentage of HAGB. The HAGB is accompanied by atomic mismatch of the alloy with higher energy between atoms. The higher energy promotes grain boundary polarization and grain refinement, which can effectively impede dislocation movement, and often leads to crack extension.

In addition, the preceding layer gets remelted and redeposited several times during build process of the subsequent layers. The solidification transformation, and the rapid cooling leads to thermal strains and volume changes within the alloy. Such complex thermal histories induce significant residual stresses in the additive sample. The combination of thermal and strain fields triggers the formation of high density dislocations [28,63]. The effect of dislocation density in MEAs can be analyzed qualitatively from the perspective of recrystallization. As shown in Fig. 10, the deformed grains (marked as red) indicate that the interior is full of dislocations; the formation of subgrain (yellow) needs

to consume and absorb some dislocations, and recrystallization (blue) has essentially no dislocation formation inside. The corresponding grain volume fractions are shown in Fig. 10(d). Combined with Fig. 9, the higher sub-grains and refinement of Al_5Ti_5 indicates that the alloy has a higher dislocation density and smaller grain size. The grain boundaries between subgrains impede the dislocation motion and restrict the plastic deformation of the MEAs. To sum up, the excellent mechanical properties of Al_5Ti_5 MEA stem from the lattice distortion-induced solid solution strengthening and grain boundary strengthening.

4. Conclusion

In this work, a novel powder plasma arc additive manufacturing (PPA-AM) has been used to fabricate $(\text{AlTi})_{2x}(\text{CoCrNi})_{100-2x}$ MEAs. Their microstructure, mechanical properties and strengthening mechanisms were investigated. The main conclusions drawn from the study are summarized as follows:

- (1) The $(\text{AlTi})_{2x}(\text{CoCrNi})_{100-2x}$ MEAs demonstrated a typical $\langle 001 \rangle$ columnar crystal structure and $\{001\}$ fiber texture along the build direction. The $\{001\}$ fiber texture characteristics gradually weaken, and the grain orientation tends to be randomized with the increase of Al and Ti.
- (2) The microhardness results showed that the average microhardness of the MEAs with Al and Ti doping increased, from 180 HV to 440 HV. The tensile yield strength exhibited an enhancement from 180 MPa for based (CoCrNi) to 808 MPa for (CoCrNi) $_{86}\text{Al}_7\text{Ti}_7$. In particular, (CoCrNi) $_{90}\text{Al}_5\text{Ti}_5$ achieved the strength-ductility balance (yield strength, tensile strength and elongation to failure of 664 MPa, 897 MPa and 19.3 %, respectively).
- (3) A direct relationship between atomic size and solid solution strengthening was observed, namely, the larger the lattice distortion the more significant the solid solution strengthening. Moreover, the increased of Al and Ti induced grain refinement of the alloys and the grain boundary strengthening increased significantly.

CRedit authorship contribution statement

Jinle Luo: Conceptualization, Methodology, Formal analysis, Software, Data curation, Writing – original draft. **Xizhang Chen:** Funding acquisition, Writing – review & editing, Supervision. **Vladislav B. Deev:** Writing – review & editing, Methodology. **Ming Wen:** Writing – review & editing, Methodology. **Yong Shen:** Supervision, Methodology. **Sergey Kononov:** Supervision, Methodology.

Declaration of Competing Interest

The authors declare that they have no known competing financial interests or personal relationships that could have appeared to influence the work reported in this paper.

Data Availability

Data will be made available on request.

Acknowledgments

This project is supported by National Natural Science Foundation of China (No. 51975419), the Scientific Research Fund of Zhejiang Provincial Education Department (No. Y202248963).

References

- [1] B. Cantor, I.T.H. Chang, P. Knight, A.J.B. Vincent, Microstructural development in equiatomic multicomponent alloys, *Mater. Sci. Eng. A* 375–377 (2004) 213–218, <https://doi.org/10.1016/j.msea.2003.10.257>.
- [2] J.-W. Yeh, S.-K. Chen, S.-J. Lin, J.-Y. Gan, T.-S. Chin, T.-T. Shun, C.-H. Tsau, S.-Y. Chang, Nanostructured high-entropy alloys with multiple principal elements: novel alloy design concepts and outcomes, *Adv. Eng. Mater.* 6 (2004) 299–303, <https://doi.org/10.1002/adem.200300567>.
- [3] Z. Zhu, T. Yang, R. Shi, X. Quan, J. Zhang, R. Qiu, B. Song, Q. Liu, The effects of annealing at different temperatures on microstructure and mechanical properties of cold-rolled $\text{Al}_{0.3}\text{CoCrFeNi}$ high-entropy alloy, *Metals* 11 (2021) 940, <https://doi.org/10.3390/met11060940>.
- [4] P. Wang, J. Chen, B. Sun, D. Zhu, Y. Cao, Effects of annealing process parameters on microstructural evolution and strength-ductility combination of CoCrFeMnNi high-entropy alloy, *Mater. Sci. Eng. A* 840 (2022), 142880, <https://doi.org/10.1016/j.msea.2022.142880>.
- [5] Y. Zhang, T.T. Zuo, Z. Tang, M.C. Gao, K.A. Dahmen, P.K. Liaw, Z.P. Lu, Microstructures and properties of high-entropy alloys, *Prog. Mater. Sci.* 61 (2014) 1–93, <https://doi.org/10.1016/j.pmatsci.2013.10.001>.
- [6] M.-H. Tsai, J.-W. Yeh, High-entropy alloys: a critical review, *Mater. Res. Lett.* 2 (2014) 107–123, <https://doi.org/10.1080/21663831.2014.912690>.
- [7] X.H. Du, W.P. Li, H.T. Chang, T. Yang, G.S. Duan, B.L. Wu, J.C. Huang, F.R. Chen, C.T. Liu, W.S. Chuang, Y. Lu, M.L. Sui, E.W. Huang, Dual heterogeneous structures lead to ultrahigh strength and uniform ductility in a Co-Cr-Ni medium-entropy alloy, *Nat. Commun.* 11 (2020) 2390, <https://doi.org/10.1038/s41467-020-16085-z>.
- [8] J.Y. He, H. Wang, Y. Wu, X.J. Liu, H.H. Mao, T.G. Nieh, Z.P. Lu, Precipitation behavior and its effects on tensile properties of FeCoNiCr high-entropy alloys, *Intermetallics* 79 (2016) 41–52, <https://doi.org/10.1016/j.intermet.2016.09.005>.
- [9] G. Liang, G. Jin, X. Cui, Z. Qiu, J. Wang, Investigation on the relationship between reinforcing behavior of TiN and wear resistance of AlCoCrCuNiTi high-entropy alloy coating, *Appl. Surf. Sci.* 593 (2022), 153419, <https://doi.org/10.1016/j.apsusc.2022.153419>.
- [10] M. Wu, K. Chen, Z. Xu, D.Y. Li, Effect of Ti addition on the sliding wear behavior of AlCrFeCoNi high-entropy alloy, *Wear* 462–463 (2020), 203493, <https://doi.org/10.1016/j.wear.2020.203493>.
- [11] Y. Guo, L. Liu, W. Zhang, K.D. Yao, W. Chen, J. Ren, J.G. Qi, B. Wang, Z.F. Zhao, J. Shang, Y. Zhang, J. Xiang, A new method for preparing high entropy alloys: electromagnetic pulse treatment and its effects on mechanical and corrosion properties, *Mater. Sci. Eng. A* 774 (2020), 138916, <https://doi.org/10.1016/j.msea.2020.138916>.
- [12] L. Huang, X. Wang, X. Zhao, C. Wang, Y. Yang, Analysis on the key role in corrosion behavior of CoCrNiAlTi-based high entropy alloy, *Mater. Chem. Phys.* 259 (2021), 124007, <https://doi.org/10.1016/j.matchemphys.2020.124007>.
- [13] J. Xu, J.Y. Zhang, Y.Q. Wang, P. Zhang, J. Kuang, G. Liu, G.J. Zhang, J. Sun, Annealing-dependent microstructure, magnetic and mechanical properties of high-entropy FeCoNiAl_{0.5} alloy, *Mater. Sci. Eng. A* 776 (2020), 139003, <https://doi.org/10.1016/j.msea.2020.139003>.
- [14] C. Zhao, J. Li, Y. Liu, W.Y. Wang, H. Kou, E. Beaugnon, J. Wang, Tailoring mechanical and magnetic properties of AlCoCrFeNi high-entropy alloy via phase transformation, *J. Mater. Sci. Technol.* 73 (2021) 83–90, <https://doi.org/10.1016/j.jmst.2020.08.063>.
- [15] Z. Wu, H. Bei, F. Otto, G.M. Pharr, E.P. George, Recovery, recrystallization, grain growth and phase stability of a family of FCC-structured multi-component equiatomic solid solution alloys, *Intermetallics* 46 (2014) 131–140, <https://doi.org/10.1016/j.intermet.2013.10.024>.
- [16] G. Laplanche, A. Kostka, C. Reinhart, J. Hunfeld, G. Eggeler, E.P. George, Reasons for the superior mechanical properties of medium-entropy CrCoNi compared to high-entropy CrMnFeCoNi, *Acta Mater.* 128 (2017) 292–303, <https://doi.org/10.1016/j.actamat.2017.02.036>.
- [17] J. Miao, C.E. Slone, T.M. Smith, C. Niu, H. Bei, M. Ghazisaeidi, G.M. Pharr, M. J. Mills, The evolution of the deformation substructure in a Ni-Co-Cr equiatomic solid solution alloy, *Acta Mater.* 132 (2017) 35–48, <https://doi.org/10.1016/j.actamat.2017.04.033>.
- [18] Y.L. Zhao, T. Yang, Y. Tong, J. Wang, J.H. Luan, Z.B. Jiao, D. Chen, Y. Yang, A. Hu, C.T. Liu, J.-J. Kai, Heterogeneous precipitation behavior and stacking-fault-mediated deformation in a CoCrNi-based medium-entropy alloy, *Acta Mater.* 138 (2017) 72–82, <https://doi.org/10.1016/j.actamat.2017.07.029>.
- [19] M.P. Agustianingrum, S. Yoshida, N. Tsuji, N. Park, Effect of aluminum addition on solid solution strengthening in CoCrNi medium-entropy alloy, *J. Alloys Compd.* 781 (2019) 866–872, <https://doi.org/10.1016/j.jallcom.2018.12.065>.
- [20] H. Peng, L. Hu, J. Chen, S. Huang, L. Li, Y. Yi, F. Zhou, W. Fang, I. Baker, Microstructures and deformation mechanisms of the medium-entropy alloy (NiCoCr) $_{76}(\text{NiAlTi})_3$, *Mater. Sci. Eng. A* 849 (2022), 143449, <https://doi.org/10.1016/j.msea.2022.143449>.
- [21] X. Liu, M. Zhang, Y. Ma, W. Dong, R. Li, Y. Lu, Y. Zhang, P. Yu, Y. Gao, G. Li, Achieving ultrahigh strength in CoCrNi-based medium-entropy alloys with synergistic strengthening effect, *Mater. Sci. Eng. A* 776 (2020), 139028, <https://doi.org/10.1016/j.msea.2020.139028>.
- [22] P. Sathiyamoorthi, J. Moon, J.W. Bae, P. Asghari-Rad, H.S. Kim, Superior cryogenic tensile properties of ultrafine-grained CoCrNi medium-entropy alloy produced by high-pressure torsion and annealing, *Scr. Mater.* 163 (2019) 152–156, <https://doi.org/10.1016/j.scriptamat.2019.01.016>.

- [23] Y. Brif, M. Thomas, I. Todd, The use of high-entropy alloys in additive manufacturing, *Scr. Mater.* 99 (2015) 93–96, <https://doi.org/10.1016/j.scriptamat.2014.11.037>.
- [24] S. Zhao, D. Xin, X. Chen, J. Stasic, M. Trtica, A.N. Siddiquee, S. Mohan, Microstructure and enhanced tensile properties of AlCoCrFeNi high entropy alloys with high Co content fabricated by laser melting deposition, *J. Alloys Compd.* 917 (2022), 165403, <https://doi.org/10.1016/j.jallcom.2022.165403>.
- [25] D. Svetlizky, M. Das, B. Zheng, A.L. Vyatskiikh, S. Bose, A. Bandyopadhyay, J. M. Schoenung, E.J. Lavernia, N. Eliaz, Directed energy deposition (DED) additive manufacturing: physical characteristics, defects, challenges and applications, *Mater. Today* 49 (2021) 271–295, <https://doi.org/10.1016/j.mattod.2021.03.020>.
- [26] Y.T. Ang, S.L. Sing, J.C.W. Lim, Process study for directed energy deposition of 316L stainless steel with TiB₂ metal matrix composites, *Mater. Sci. Addit. Manuf.* 1 (2022) 13, <https://doi.org/10.18063/msam.v1i2.13>.
- [27] A. Ostovari Moghaddam, N.A. Shaburova, M.N. Samodurova, A. Abdollahzadeh, E. A. Trofimov, Additive manufacturing of high entropy alloys: a practical review, *J. Mater. Sci. Technol.* 77 (2021) 131–162, <https://doi.org/10.1016/j.jmst.2020.11.029>.
- [28] Z. Liu, D. Zhao, P. Wang, M. Yan, C. Yang, Z. Chen, J. Lu, Z. Lu, Additive manufacturing of metals: microstructure evolution and multistage control, *J. Mater. Sci. Technol.* 100 (2022) 224–236, <https://doi.org/10.1016/j.jmst.2021.06.011>.
- [29] Z.G. Zhu, Q.B. Nguyen, F.L. Ng, X.H. An, X.Z. Liao, P.K. Liaw, S.M.L. Nai, J. Wei, Hierarchical microstructure and strengthening mechanisms of a CoCrFeNiMn high entropy alloy additively manufactured by selective laser melting, *Scr. Mater.* 154 (2018) 20–24, <https://doi.org/10.1016/j.scriptamat.2018.05.015>.
- [30] S. Luo, C. Zhao, Y. Su, Q. Liu, Z. Wang, Selective laser melting of dual phase AlCrCuFeNi high entropy alloys: formability, heterogeneous microstructures and deformation mechanisms, *Addit. Manuf.* 31 (2020), 100925, <https://doi.org/10.1016/j.addma.2019.100925>.
- [31] P. Xue, L. Zhu, P. Xu, H. Lu, S. Wang, Z. Yang, J. Ning, S.L. Sing, Y. Ren, Effect of heat treatment on microstructure and mechanical properties of in-situ synthesized Ni₂CrCoNb_{0.16} multi-principal element alloy manufactured by directed energy deposition, *Mater. Sci. Eng. A* 862 (2023), 144398, <https://doi.org/10.1016/j.msea.2022.144398>.
- [32] H. Peng, S. Xie, P. Niu, Z. Zhang, T. Yuan, Z. Ren, X. Wang, Y. Zhao, R. Li, Additive manufacturing of Al_{0.3}CoCrFeNi high-entropy alloy by powder feeding laser melting deposition, *J. Alloys Compd.* 862 (2021), 158286, <https://doi.org/10.1016/j.jallcom.2020.158286>.
- [33] A. Farzaneh, M. Khorasani, E. Farabi, I. Gibson, M. Leary, A. Ghasemi, B. Rolfe, Sandwich structure printing of Ti-Ni-Ti by directed energy deposition, *Virtual Phys. Prototyp.* 17 (2022) 1006–1030, <https://doi.org/10.1080/17452759.2022.2096647>.
- [34] K. Kuwabara, H. Shiratori, T. Fujieda, K. Yamanaka, Y. Koizumi, A. Chiba, Mechanical and corrosion properties of AlCoCrFeNi high-entropy alloy fabricated with selective electron beam melting, *Addit. Manuf.* 23 (2018) 264–271, <https://doi.org/10.1016/j.addma.2018.06.006>.
- [35] N. Li, S. Huang, G. Zhang, R. Qin, W. Liu, H. Xiong, G. Shi, J. Blackburn, Progress in additive manufacturing on new materials: a review, *J. Mater. Sci. Technol.* 35 (2019) 242–269, <https://doi.org/10.1016/j.jmst.2018.09.002>.
- [36] B. Dong, Z. Wang, Z. Pan, O. Muránsky, C. Shen, M. Reid, B. Wu, X. Chen, H. Li, On the development of pseudo-eutectic AlCoCrFeNi_{2.1} high entropy alloy using powder-bed arc additive manufacturing (PAAM) process, *Mater. Sci. Eng. A* 802 (2021), 140639, <https://doi.org/10.1016/j.msea.2020.140639>.
- [37] P. Niu, R. Li, K. Gan, T. Yuan, S. Xie, C. Chen, Microstructure, properties, and metallurgical defects of an equimolar CoCrNi medium entropy alloy additively manufactured by selective laser melting, *Metall. Mater. Trans. A* 52 (2021) 753–766, <https://doi.org/10.1007/s11661-020-06121-4>.
- [38] B. Han, C. Zhang, K. Feng, Z. Li, X. Zhang, Y. Shen, X. Wang, H. Kokawa, R. Li, Z. Wang, P.K. Chu, Additively manufactured high strength and ductility CrCoNi medium entropy alloy with hierarchical microstructure, *Mater. Sci. Eng. A* 820 (2021), 141545, <https://doi.org/10.1016/j.msea.2021.141545>.
- [39] P. Xue, L. Zhu, P. Xu, H. Lu, S. Wang, Z. Yang, J. Ning, S.L. Sing, Y. Ren, Microstructure evolution and enhanced mechanical properties of additively manufactured CrCoNi medium-entropy alloy composites, *J. Alloys Compd.* 928 (2022), 167169, <https://doi.org/10.1016/j.jallcom.2022.167169>.
- [40] Y. Zhang, X. Chen, S. Jayalakshmi, R.A. Singh, V.B. Deev, E.S. Prusov, Factors determining solid solution phase formation and stability in CoCrFeNiX_{0.4} (X=Al, Nb, Ta) high entropy alloys fabricated by powder plasma arc additive manufacturing, *J. Alloys Compd.* 857 (2021), 157625, <https://doi.org/10.1016/j.jallcom.2020.157625>.
- [41] Q. Shen, J. Xue, Z. Zheng, X. Yu, N. Ou, Effect of heat treatment on microstructure and mechanical properties of Al_{1.2}CoCrFeNi_{2.1} high-entropy alloy fabricated by powder plasma arc additive manufacturing, *Mater. Sci. Eng. A* 857 (2022), 144129, <https://doi.org/10.1016/j.msea.2022.144129>.
- [42] Y. Li, Y. Hu, D. Zhang, W. Cong, Laser remelting of CoCrFeNiTi high entropy alloy coatings fabricated by directed energy deposition: effects of remelting laser power, *Opt. Laser Technol.* 158 (2023), 108871, <https://doi.org/10.1016/j.optlastec.2022.108871>.
- [43] Q. Sui, Z. Wang, J. Wang, S. Xu, Q. Yuan, H. Wen, T. Xiao, J. Liu, Phase evolution and mechanical properties of AlxCoCrFeNi high-entropy alloys by directed energy deposition, *Mater. Charact.* 204 (2023), 113217, <https://doi.org/10.1016/j.matchar.2023.113217>.
- [44] S. Liu, C.M. Grohol, Y.C. Shin, High throughput synthesis of CoCrFeNiTi high entropy alloys via directed energy deposition, *J. Alloys Compd.* 916 (2022), 165469, <https://doi.org/10.1016/j.jallcom.2022.165469>.
- [45] Y. Chen, Q. Zhou, Directed energy deposition additive manufacturing of CoCrFeMnNi high-entropy alloy towards densification, grain structure control and improved tensile properties, *Mater. Sci. Eng. A* 860 (2022), 144272, <https://doi.org/10.1016/j.msea.2022.144272>.
- [46] W. Lu, X. Luo, Y. Yang, J. Zhang, B. Huang, Effects of Al addition on structural evolution and mechanical properties of the CrCoNi medium-entropy alloy, *Mater. Chem. Phys.* 238 (2019), 121841, <https://doi.org/10.1016/j.matchemphys.2019.121841>.
- [47] R. Li, P. Niu, T. Yuan, P. Cao, C. Chen, K. Zhou, Selective laser melting of an equiatomic CoCrFeMnNi high-entropy alloy: processability, non-equilibrium microstructure and mechanical property, *J. Alloys Compd.* 746 (2018) 125–134, <https://doi.org/10.1016/j.jallcom.2018.02.298>.
- [48] H. Jung, J. Lee, G.H. Gu, H. Lee, S.-M. Seo, A. Zargaran, H.S. Kim, S.S. Sohn, Multiscale defects enable synergetic improvement in yield strength of CrCoNi-based medium-entropy alloy fabricated via laser-powder bed fusion, *Addit. Manuf.* 61 (2023), 103360, <https://doi.org/10.1016/j.addma.2022.103360>.
- [49] M. Zheng, C. Li, X. Zhang, Z. Ye, Y. Liao, J. Gu, Design of a novel (CoCrNi)_{84.5}Al_{15.5} eutectic medium-entropy alloy with hierarchically nano-lamellar microstructure through additively manufactured compositionally graded materials, *Mater. Sci. Eng. A* 878 (2023), 145209, <https://doi.org/10.1016/j.msea.2023.145209>.
- [50] Z. Li, P. Zhao, T. Lu, K. Feng, Y. Tong, B. Sun, N. Yao, Y. Xie, B. Han, X. Zhang, S. Tu, Effects of post annealing on the microstructure, precipitation behavior, and mechanical property of a (CoCrNi)₉₄Al₃Ti₃ medium-entropy alloy fabricated by laser powder bed fusion, *J. Mater. Sci. Technol.* 135 (2023) 142–155, <https://doi.org/10.1016/j.jmst.2022.07.012>.
- [51] J. Fu, H. Li, X. Song, M.W. Fu, Multi-scale defects in powder-based additively manufactured metals and alloys, *J. Mater. Sci. Technol.* 122 (2022) 165–199, <https://doi.org/10.1016/j.jmst.2022.02.015>.
- [52] M. Karimzadeh, M. Malekan, H. Mirzadeh, L. Li, N. Saini, Effects of titanium addition on the microstructure and mechanical properties of quaternary CoCrFeNi high entropy alloy, *Mater. Sci. Eng. A* 856 (2022), 143971, <https://doi.org/10.1016/j.msea.2022.143971>.
- [53] X.B. Feng, W. Fu, J.Y. Zhang, J.T. Zhao, J. Li, K. Wu, G. Liu, J. Sun, Effects of nanotwins on the mechanical properties of Al x CoCrFeNi high entropy alloy thin films, *Scr. Mater.* 139 (2017) 71–76, <https://doi.org/10.1016/j.scriptamat.2017.06.009>.
- [54] Z. Yan, D. Wang, X. He, W. Wang, H. Zhang, P. Dong, C. Li, Y. Li, J. Zhou, Z. Liu, L. Sun, Deformation behaviors and cyclic strength assessment of AZ31B magnesium alloy based on steady ratcheting effect, *Mater. Sci. Eng. A* 723 (2018) 212–220, <https://doi.org/10.1016/j.msea.2018.03.023>.
- [55] X. Ma, C. Huang, J. Moering, M. Ruppert, H.W. Höppel, M. Göken, J. Narayan, Y. Zhu, Mechanical properties of copper/bronze laminates: role of interfaces, *Acta Mater.* 116 (2016) 43–52, <https://doi.org/10.1016/j.actamat.2016.06.023>.
- [56] M. Yang, D. Yan, F. Yuan, P. Jiang, E. Ma, X. Wu, Dynamically reinforced heterogeneous grain structure prolongs ductility in a medium-entropy alloy with gigapascal yield strength, *Proc. Natl. Acad. Sci.* 115 (2018) 7224–7229, <https://doi.org/10.1073/pnas.1807817115>.
- [57] Y. Xie, P. Zhao, Y. Tong, J. Tan, B. Sun, Y. Cui, R. Wang, X. Zhang, S. Tu, Precipitation and heterogeneous strengthened CoCrNi-based medium entropy alloy with excellent strength-ductility combination from room to cryogenic temperatures, *Sci. China Technol. Sci.* 65 (2022) 1780–1797, <https://doi.org/10.1007/s11431-022-2076-1>.
- [58] F. Hamdi, S. Asgari, Evaluation of the role of deformation twinning in work hardening behavior of face-centered-cubic polycrystals, *Metall. Mater. Trans. A* 39 (2008) 294–303, <https://doi.org/10.1007/s11661-007-9356-6>.
- [59] B. Hutchinson, N. Ridley, On dislocation accumulation and work hardening in Hadfield steel, *Scr. Mater.* 55 (2006) 299–302, <https://doi.org/10.1016/j.scriptamat.2006.05.002>.
- [60] H. Chang, T.W. Zhang, S.G. Ma, D. Zhao, R.L. Xiong, T. Wang, Z.Q. Li, Z.H. Wang, Novel Si-added CrCoNi medium entropy alloys achieving the breakthrough of strength-ductility trade-off, *Mater. Des.* 197 (2021), 109202, <https://doi.org/10.1016/j.matdes.2020.109202>.
- [61] Y. Zhang, Q. Shen, X. Chen, S. Jayalakshmi, R.A. Singh, S. Kononov, V.B. Deev, E. S. Prusov, Strengthening mechanisms in CoCrFeNiX_{0.4} (Al, Nb, Ta) high entropy alloys fabricated by powder plasma arc additive manufacturing, *Nanomaterials* 11 (2021) 721, <https://doi.org/10.3390/nano11030721>.
- [62] G. Zheng, X. Mao, L. Li, R. Dang, The variation of microstructures, textures and mechanical properties from edge to center in cross section of Ti6242s titanium alloy, *Vacuum* 160 (2019) 81–88, <https://doi.org/10.1016/j.vacuum.2018.09.046>.
- [63] N. Raghavan, S. Simunovic, R. Dehoff, A. Plotkowski, J. Turner, M. Kirka, S. Babu, Localized melt-scan strategy for site specific control of grain size and primary dendrite arm spacing in electron beam additive manufacturing, *Acta Mater.* 140 (2017) 375–387, <https://doi.org/10.1016/j.actamat.2017.08.038>.